

# Energy dependence of fission-fragment mass distributions from strongly damped shape evolution

J. Randrup<sup>1</sup> and P. Möller<sup>2</sup>

<sup>1</sup>*Nuclear Science Division, Lawrence Berkeley National Laboratory, Berkeley, California 94720, USA*

<sup>2</sup>*Theoretical Division, Los Alamos National Laboratory, Los Alamos, New Mexico 87545, USA*

(Received 18 July 2013; published 10 December 2013)

The recently developed treatment of Brownian shape evolution is refined to take account of the gradual decrease in microscopic effects as the nuclear excitation energy is raised. We construct effective potential-energy surfaces by multiplying the shell-plus-pairing correction term by a suppression factor that depends on the local excitation energy. While this approach is equivalent to the modification of the Fermi-gas level density parameter suggested by Ignatyuk *et al.* [Sov. J. Nucl. Phys. **29**, 450 (1979)], we adopt a more general functional form for the suppression factor, which is adjusted to measured charge yields for <sup>234</sup>U ( $E^* \approx 11$  MeV). The resulting model is benchmarked by comparison with 70 measured yields.

DOI: 10.1103/PhysRevC.88.064606

PACS number(s): 25.85.-w, 21.60.-n, 24.10.Lx

## I. INTRODUCTION

The approximate treatment of nuclear shape evolutions in terms of Metropolis walks on five-dimensional (5D) potential-energy surfaces has been remarkably successful for predicting fission-fragment mass distributions [1–3]. However, until now, the treatment has not taken account of the gradual weakening of the shell and pairing corrections as the nuclear excitation energy is raised. The present study models this feature by means of energy-dependent effective potential-energy surfaces.

In Sec. II, we briefly review the key features of the Metropolis method, and then, in Sec. III, we discuss our treatment of the energy dependence. Finally, in Sec. IV, we benchmark the refined treatment against experimental data for 70 fission-fragment yields.

## II. BROWNIAN SHAPE MOTION

In the Metropolis walk treatment, the formal starting point is the commonly employed Langevin framework [4], which treats the time development of the multidimensional nuclear shape as it responds to the driving force from the potential energy of deformation and the dissipative force due to the interaction between the shape degrees of freedom and the residual part of the nuclear many-body system.

Specifically, in the present approach, the shape is parametrized in terms of the three-quadratic-surface family introduced by Nix [5,6]. The associated five-dimensional shape “coordinate” is denoted here by  $\chi = \{\chi_i\}$  with  $i = 1, \dots, 5$ . For over five thousand nuclei, the potential-energy landscape was calculated [7] by use of the macroscopic-microscopic method [8,9] which provides the energy of a given shape on the form  $U(\chi) = U_{\text{macro}}(\chi) + U_{\text{sh+pair}}(\chi)$ . The first term was obtained with the finite-range liquid-drop model, and the second term represents the microscopic shell and pairing corrections [7]. The resulting driving force is then  $\mathbf{F}^{\text{pot}}(\chi) = -\partial U(\chi)/\partial \chi$ , and the kinetic energy associated with a shape change is given by  $K(\dot{\chi}, \chi) = \frac{1}{2} \sum_{ij} M_{ij}(\chi) \dot{\chi}_i \dot{\chi}_j$ , where  $\mathbf{M}(\chi)$  is the  $5 \times 5$  inertial-mass tensor. The Lagrangian function for the shape dynamics is, thus,  $\mathcal{L}(\dot{\chi}, \chi) = K(\dot{\chi}, \chi) - U(\chi)$ .

The dissipative coupling between the shape and the microscopic degrees of freedom is encoded into the  $5 \times 5$  dissipation tensor  $\gamma(\dot{\chi}, \chi)$  in terms of which the Rayleigh function is expressed:  $\mathcal{F}(\dot{\chi}, \chi) = \frac{1}{2} \sum_{ij} \gamma_{ij}(\chi) \dot{\chi}_i \dot{\chi}_j$ . The average dissipative effect produces a friction force  $\mathbf{F}^{\text{fric}}(\dot{\chi}, \chi) = -\partial \mathcal{F}(\chi)/\partial \dot{\chi}$  [whose five components are  $F_i^{\text{fric}}(\dot{\chi}, \chi) = -\sum_j \gamma(\chi)_{ij} \dot{\chi}_j$ ], while the residual dissipative effect is represented by a stochastic force  $\mathbf{F}^{\text{ran}}(\chi; t)$ , which gives the evolution of  $\chi$  a diffusive character. The random force varies relatively rapidly in time and is assumed to be Markovian, i.e.,  $\langle \mathbf{F}^{\text{ran}}(\chi; t) \mathbf{F}^{\text{ran}}(\chi; t') \rangle = 2T(\chi) \gamma_{ij}(\chi) \delta(t - t')$ , where  $T(\chi)$  is the shape-dependent temperature (see below). The total dissipative force is thus  $\mathbf{F}^{\text{diss}} = \mathbf{F}^{\text{fric}} + \mathbf{F}^{\text{ran}}$ .

The Langevin equation of motion for the evolution of the five-dimensional shape parameter  $\chi$  is given by

$$\frac{d}{dt} \frac{\partial}{\partial \dot{\chi}} \mathcal{L}(\dot{\chi}, \chi) = \frac{\partial}{\partial \chi} \mathcal{L}(\dot{\chi}, \chi) + \mathbf{F}^{\text{diss}}(\chi; t). \quad (1)$$

Relative to this general description, the key simplifying assumption in our treatment is that the dissipative coupling is sufficiently strong to render the inertial-mass tensor  $\mathbf{M}(\chi)$  unimportant. The term on the left-hand side of Eq. (1) is then absent, and the Langevin equation reduces to the Smoluchowski equation in which there are no inertial forces. Consequently, the shape dynamics is determined by the balancing of the driving force against the dissipative force  $\mathbf{F}^{\text{pot}} + \mathbf{F}^{\text{diss}} \doteq \mathbf{0}$ . This condition yields the instantaneous rate of shape change,

$$\dot{\chi}(\chi; t) = \boldsymbol{\mu}(\chi) \cdot [\mathbf{F}^{\text{pot}}(\chi) + \mathbf{F}^{\text{ran}}(\chi; t)], \quad (2)$$

where  $\boldsymbol{\mu}(\chi) \equiv \boldsymbol{\gamma}(\chi)^{-1}$  is the shape dependent  $5 \times 5$  mobility tensor. Thus, the net change in  $\chi$  in the course of a brief time interval  $\Delta t$  consists of a deterministic part that represents the average change,  $\boldsymbol{\mu} \cdot \mathbf{F}^{\text{pot}} \Delta t$ , and a stochastic part proportional to the square root of  $T$  and  $\Delta t$ . It is straightforward to numerically simulate the resulting diffusive evolution of the nuclear shape [2].

This type of dynamics is characteristic of Brownian motion, the erratic movements of a particle immersed in a fluid. But relative to the standard scenario where the fluid is

three-dimensional, uniform, isotropic, and force free, the nuclear Brownian shape dynamics is more complex: The “particle” (the nuclear shape) moves in a five-dimensional space, it is subject to an external force (the driving force  $\mathbf{F}^{\text{pot}}$ ), which is nonuniform (it depends on the shape parameter  $\chi$ ), and the interaction with the medium (described by the dissipation tensor  $\gamma$ ) is both nonuniform ( $\gamma$  depends on  $\chi$ ) and anisotropic (the five eigenvalues of  $\gamma$  are not equal, nor are the eigenvectors aligned with the  $\chi$  coordinate system).

In order to calculate the fission-fragment mass distribution, one typically proceeds as follows. The Brownian motion on the potential-energy surface is started from a suitably compact shape, such as the ground-state shape or an isomeric minimum; the precise starting point is immaterial as long as it is located well inside the highest saddle. The resulting track is then followed until the system has passed beyond the last barrier and is well on its way towards scission. At this stage, the nuclear shape has developed a binary character with the two parts being joined by a relatively small neck. Any further change in the mass asymmetry is then strongly suppressed, so the evolution is terminated, and the current mass asymmetry is binned. With this procedure, a sufficiently large number of individual tracks (typically 10 000) are generated to produce a good-quality histogram of the resulting fission-fragment mass yield  $Y(A_f)$ .

The strong dissipation causes the shape to evolve rather slowly, and it may, therefore, be expected that a high degree of relaxation occurs along the evolution towards scission. Consequently, the sensitivity to the specific form of the dissipation tensor  $\gamma$  should be diminished, and it was found that the resulting fragment mass distributions are, indeed, relatively insensitive to the structure of  $\gamma$  [2]. This provides a justification for the method introduced in Ref. [1], namely, that the shape evolution may be simulated by means of a Metropolis walk on the five-dimensional  $\chi$  lattice where the potential  $U$  is available [7] because this procedure generates the shape evolutions implied by the Smoluchowski equation (2) for the extreme case of an isotropic diffusion tensor,  $\gamma_{ij}(\chi) = \gamma_0(\chi) \delta_{ij}$  [1].

The original Metropolis procedure was developed to generate a sequence of lattice sites  $\{\chi_n\}$  that are distributed according to the applicable statistical weight  $W(\chi)$  [10]. [For a canonical distribution of temperature  $T$ , the statistical weight is given by  $W(\chi) \sim \exp(-U(\chi)/T)$ .] Having arrived at shape number  $n$  in the sequence  $\{\chi_n\}$ , one determines the next shape in the sequence as follows. First one of the neighboring shapes  $\chi'$  is selected randomly, and its statistical weight  $W(\chi')$  is compared with that of the current shape,  $W(\chi_n)$ . If the candidate shape  $\chi'$  has a larger statistical weight, then it is accepted as the next shape in the sequence, i.e.,  $\chi_{n+1} = \chi'$ . But if the candidate shape has a smaller statistical weight, it is accepted only with the probability  $W(\chi')/W(\chi_n)$  (in which case,  $\chi_{n+1} = \chi'$ ), whereas the shape  $\chi_n$  is taken as shape number  $n + 1$  otherwise (in which case the current shape is repeated  $\chi_{n+1} = \chi_n$ ). The Metropolis procedure, thus, produces a diffusive random walk through the shape lattice, and it is easy to verify that, for a closed system, the selected lattice shapes  $\{\chi_n\}$  are distributed in accordance with the statistical weight  $W(\chi)$ . However, in the present case, the

system is not closed, and only partial equilibration occurs before scission is reached.

The generation of the Metropolis walks on the shape lattice is computationally far less demanding than the numerical solution of the Smoluchowski equation with a nontrivial dissipation tensor. The method, therefore, presents a very powerful tool for making approximate (but essentially parameter-free) predictions of fragment mass distributions. However, it should be noted that the Metropolis walk only provides the tracks through the shape lattice but not any temporal information (i.e., it provides the *shape* evolution but not the *time* evolution) but that suffices for calculating the mass splits.

In applications up to now, the statistical weight was taken as  $W(\chi) \sim \exp[-U(\chi)/T(\chi)]$ , where  $T(\chi)$  is the local temperature, i.e., the temperature of the nucleus when its shape is as specified by  $\chi$ . When the energy of the fissioning system is increased, the local temperatures increase correspondingly and that, in turn, broadens the resulting mass distribution. However, the increase in the nuclear excitation energy also causes the microscopic effects to gradually subside. This behavior can be of considerable significance but was not accounted for previously. Therefore, in the present paper, we address this issue and show how the gradual disappearance of microscopic effects may be included in a simple approximate manner by means of energy-dependent potential-energy surfaces.

### III. TREATMENT OF ENERGY DEPENDENCE

The potential energies were calculated [7] with the macroscopic-microscopic method, so they have the form

$$U(\chi) = U_{\text{macro}}(\chi) + U_{\text{sh+pair}}(\chi), \quad (3)$$

where both terms are available on a five-dimensional lattice of shapes  $\chi$ . The macroscopic energy was calculated by means of the finite-range liquid-drop model [11,12] and depends smoothly on deformation, as illustrated in Fig. 1 (solid curve in the upper panel). The corresponding macroscopic potential-energy landscape,  $U_{\text{macro}}(\chi)$ , displays a single saddle point, and the associated shape is reflection symmetric. By contrast, the microscopic part of the energy tends to exhibit an undulatory behavior as the shape is changed (dashed curve in the upper panel of Fig. 1). As a consequence, the total potential-energy landscape,  $U(\chi)$  (solid curve in the lower panel), has a rather bumpy appearance, which, for the actinides, causes the ground-state shape to be deformed, generates a secondary minimum, and renders the outer saddle shapes reflection asymmetric.

The microscopic part of the potential energy,  $U_{\text{sh+pair}}(\chi)$ , arises from the nonuniformities in the neutron and proton single-particle level distributions near the respective Fermi surfaces. Accordingly,  $U_{\text{sh+pair}}(\chi)$  vanishes when the level spectra are regular. We denote the density of nuclear many-body states for this reference scenario by  $\bar{\rho}(E^*)$ , where  $E^*$  is the nuclear excitation energy, measured relative to the potential energy of the given shape  $\chi$ ,  $E^*(\chi) = E - U(\chi)$ , with  $E$  being the total energy. Usually, it is taken to have a simplified Fermi-gas form,  $\bar{\rho}(E^*) \sim \exp(2\sqrt{a}E^*)$ , where the

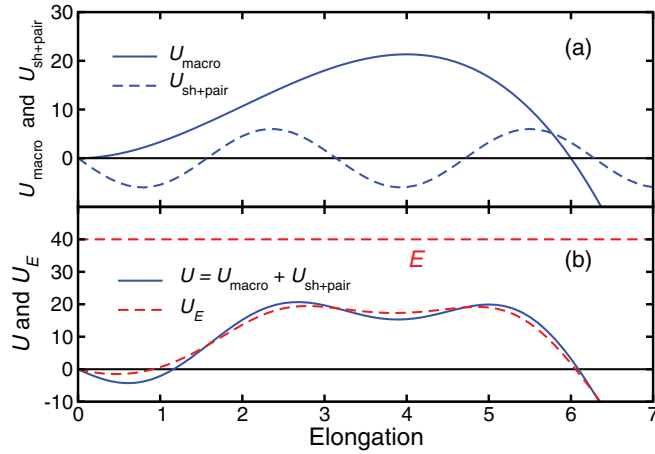


FIG. 1. (Color online) Schematic illustration of the construction of the effective potential  $U_E(\chi)$ . Panel (a): The smooth macroscopic energy  $U_{\text{macro}}$  (solid curve) and the undulating shell-plus-pairing correction  $U_{\text{sh+pair}}$  (dashed curve). Panel (b): The total potential  $U = U_{\text{macro}} + U_{\text{sh+pair}}$  (solid curve); for a given shape, the excitation energy is given by  $E^* = E - U$ , where  $E$  is the specified total energy (dashed line), and the effective potential is given by  $U_E = U_{\text{macro}} + \mathcal{S}(E^*)U_{\text{sh+pair}}$  (dashed line) and thus approaches  $E_{\text{macro}}$  for large  $E^*$ .

level-density parameter has a macroscopic form [we use  $\tilde{a} = A/(8 \text{ MeV})$ ]. The inverse of the corresponding temperature  $\tilde{T}(\chi)$  is then given by  $\tilde{\beta}(\chi) = \partial \ln \tilde{\rho}(E^*)/\partial E^*$ , which leads to the familiar expression  $E^* = \tilde{a}\tilde{T}^2$  for the simple Fermi-gas form.

The global use of the simplified Fermi-gas level density is only a rough approximation which, among other things, neglects the influence of pairing correlations. However, in view of the approximative nature of the Metropolis walk method, a more refined form does not seem warranted at this stage. A recent discussion of the influence of pairing on nuclear level densities was given in Ref. [13].

The tabulated potential energies  $U(\chi)$  pertain to a cold nucleus,  $T = 0$ . As the temperature is raised, both terms in Eq. (3) generally change. But the macroscopic term depends only weakly on temperature and is assumed to remain unchanged. On the other hand, the microscopic term exhibits a significant temperature dependence and generally subsides as the temperature is increased; it is this feature that we wish to take into account in a simple manner.

Although it would, in principle, be straightforward to recalculate the shell-plus-pairing correction for specified finite temperatures, this would, in practice, be a rather formidable task if carried out for all of the over five million shapes of more than five thousand nuclei for which the original tabulation [7] was performed. We therefore seek to develop an approximate treatment that can be implemented with the currently available information.

### A. Effective potential

For a specified total energy  $E$ , which is assumed to remain constant as the nuclear shape evolves, we introduce an energy-dependent *effective potential*  $U_E(\chi)$  by suppressing

the microscopic term by a factor  $\mathcal{S}(E^*)$  that depends on the local excitation energy  $E^*(\chi) = E - U(\chi)$ ,

$$U_E(\chi) \equiv U_{\text{macro}}(\chi) + \mathcal{S}[E^*(\chi)]U_{\text{sh+pair}}(\chi). \quad (4)$$

The characteristic energy scales for the damping of the pairing and shell corrections generally differ, so it might appear unjustified to employ a common suppression factor. However, the pairing correction usually is substantially smaller than the shell correction, and so the use of a single suppression factor is a reasonable approximation at this stage.

Because the suppression accounts for the damping of the shell-plus-pairing correction relative to its value at zero excitation, we have, by definition,  $\mathcal{S}(0) = 1$ . Furthermore,  $\mathcal{S}(E^*)$  approaches zero in the limit of high excitation. Then for zero temperature the real potential  $U$  is recovered, whereas only its macroscopic part remains at very high temperatures. The specific functional form of  $\mathcal{S}(E^*)$  will be discussed in Sec. III D.

We also define the corresponding *effective excitation energy* as the difference between the total energy and the effective potential,

$$\begin{aligned} E_E^*(\chi) &\equiv E - U_E(\chi) = \mathcal{F}_E(\chi)E^*(\chi) \\ &= E^*(\chi) + \{1 - \mathcal{S}[E^*(\chi)]\}U_{\text{sh+pair}}(\chi), \end{aligned} \quad (5)$$

where we have introduced the modification factor,

$$\begin{aligned} \mathcal{F}_E(\chi) &\equiv E_E^*(\chi)/E^*(\chi) \\ &= 1 + \{1 - \mathcal{S}[E - U(\chi)]\} \frac{U_{\text{sh+pair}}(\chi)}{E - U(\chi)}. \end{aligned} \quad (6)$$

It has the following limiting behaviors:

$$E^* \rightarrow 0 : \mathcal{F}_E \approx 1 - U_{\text{sh+pair}}\mathcal{S}'(0), \quad (7)$$

$$E^* \rightarrow \infty : \mathcal{F}_E \approx 1 + U_{\text{sh+pair}}/E^* \rightarrow 1, \quad (8)$$

where  $\mathcal{S}'(0) \equiv [\partial \mathcal{S}(E^*)/\partial E^*]_{E^*=0}$  is the initial slope of the suppression factor (which is negative). The relationship between the various potential energies is illustrated schematically in Fig. 1.

For the given total energy  $E$ , the domain of accessible shapes is determined by the condition that the local potential should be lower than the total energy:  $U(\chi) < E$ , so that the local excitation energy is positive:  $E^*(\chi) > 0$ . So the domain boundary is characterized by  $E^*(\chi) = 0$ , i.e.,  $U(\chi) = E$ . This implies that the suppression factor  $\mathcal{S}$  is unity on the boundary and so is the modification factor  $\mathcal{F}_E$ , ensuring that the effective excitation also vanishes on the domain boundary,  $E_E^*(\chi) = 0$ , i.e.,  $U_E(\chi) = E$ .

For the effective excitation  $E_E^*(\chi)$  to remain positive inside the domain boundary (where  $E^* > 0$ ), we must demand that the modification factor  $\mathcal{F}_E(\chi)$  be positive. Near the domain boundary, this condition leads to the requirement that  $U_{\text{sh+pair}}(\chi)\mathcal{S}'(0) < 1$  [see Eq. (7)], which limits how rapidly the function  $\mathcal{S}(E^*)$  may decrease initially. For example, in the case of  $\mathcal{S}(E^*) = \exp(-E^*/E_{\text{damp}})$  [14], it follows that the damping energy  $E_{\text{damp}}$  must exceed the absolute value of the most negative value of the shell-plus-pairing correction.

### B. Level density

We now assume that the energy dependence of the many-body level density can be accounted for by simply evaluating the macroscopic level density  $\tilde{\rho}(E^*)$  at the *effective* excitation energy  $E_E^* = E - U_E$ ,

$$\rho_E(\chi) = \tilde{\rho}[E_E^*(\chi)] = \tilde{\rho}[\mathcal{F}_E(\chi)E^*(\chi)]. \quad (9)$$

Thus, at high excitations, where the factor  $\mathcal{F}_E$  is unity, there is no change relative to the earlier treatment which used  $\rho = \tilde{\rho}(E^*)$  for all  $E^*$ . But  $\mathcal{F}_E$  generally deviates from unity at lower excitations, and the expression  $\tilde{\rho}(E_E^*)$  may then differ significantly from  $\tilde{\rho}(E^*)$ .

When the simple Fermi-gas form is used for  $\tilde{\rho}(E^*)$ , the prescription (9) yields

$$\rho_E(\chi) \sim \exp[2\sqrt{\tilde{a}\mathcal{F}_E(\chi)E^*(\chi)}]. \quad (10)$$

Because the product  $\tilde{a} \times \mathcal{F}_E E^*$  is equal to  $\tilde{a}\mathcal{F}_E \times E^*$ , the level-density (10) can also be written as

$$\rho_E(\chi) \sim \exp[2\sqrt{a_E(\chi)E^*(\chi)}], \quad (11)$$

where the energy-dependent *effective* level-density parameter  $a_E$  is defined by

$$a_E(\chi) \equiv \tilde{a}\mathcal{F}_E(\chi). \quad (12)$$

It approaches  $\tilde{a}[1 + U_{\text{sh+pair}}(\chi)S'(0)]$  for  $E^* \rightarrow 0$ , whereas it tends to  $\tilde{a}$  for large  $E^*$ . We note that if the suppression function is taken to be purely exponential,  $S(E^*) = \exp(-E^*/E_{\text{damp}})$ , then the expressions (11) and (12) correspond to what was employed previously by Ignatyuk *et al.* [14].

It is thus equally valid to take account of the shell structure in the single-particle level spectrum by either an energy-dependent effective level-density parameter  $a_E$  or by an energy-dependent effective excitation energy  $E_E^*$  obtained by means of an effective potential. In either case,

$$\rho_E(\chi) \sim \exp[2\sqrt{\tilde{a}\mathcal{F}_E(\chi)[E - U(\chi)]}]. \quad (13)$$

Once the level density  $\rho_E(\chi)$  is given, the various thermodynamic quantities of interest can be determined. Of particular interest is the local temperature,  $T_E(\chi)$ , whose inverse is given by [see Eq. (5)]

$$\begin{aligned} \beta_E(\chi) &= \frac{\partial}{\partial E} \ln \rho_E(\chi) = \left[ \frac{\partial}{\partial E^*} \ln \tilde{\rho}(E^*) \right]_{E_E^*} \frac{\partial E_E^*}{\partial E} \\ &= \tilde{\beta}[E_E^*(\chi)] \{1 - U_{\text{sh+pair}}(\chi)S'[E^*(\chi)]\}. \end{aligned} \quad (14)$$

Defined earlier, the function  $\tilde{\beta}(\varepsilon) \equiv \partial \ln \tilde{\rho}(\varepsilon)/\partial \varepsilon = \sqrt{\tilde{a}/\varepsilon}$  is the inverse temperature associated with the macroscopic level density  $\tilde{\rho}(\varepsilon) \sim \exp[2\sqrt{\tilde{a}\varepsilon}]$ . Thus the actual inverse temperature  $\beta_E$  is obtained by evaluating the macroscopic inverse temperature  $\tilde{\beta}$  at the effective excitation energy  $E_E^*$  and then multiplying by the factor in the square brackets in Eq. (14), which arises from the energy dependence of the effective level-density parameter  $a_E$ . It is convenient to introduce the local *effective temperature* [see Eq. (18)] defined as

$$T_{\text{eff}}(\chi) \equiv 1/\tilde{\beta}[E_E^*(\chi)] = [E_E^*(\chi)/\tilde{a}]^{1/2}. \quad (15)$$

### C. Metropolis walk

In the simple treatment introduced in Ref. [1], the Smoluchowski evolution for the nuclear shape evolution is simulated as a Metropolis walk on the 5D lattice where the potential energy  $U(\chi)$  is available. The lattice shapes are labeled by the five-dimensional site index  $\mathbf{v} = (i, j, k, l, m)$  (so the associated shape parameter  $\chi^{(\mathbf{v})}$  has the components  $\chi_1^{(\mathbf{v})} = i, \chi_2^{(\mathbf{v})} = j, \dots, \chi_5^{(\mathbf{v})} = m$ ), and the Metropolis process then provides a sequence of lattice sites,  $\{\mathbf{v}\}$ , selected as follows.

At any given stage in the walk, let the current site have the index  $\mathbf{v}$ . To determine the next index in the sequence, a candidate index  $\mathbf{v}'$  is first selected randomly (with even probability) from the neighboring sites. If the statistical weight of the selected candidate shape exceeds that of the current one,  $\Omega(\mathbf{v}') > \Omega(\mathbf{v})$ , then  $\mathbf{v}'$  is accepted as the next index in the sequence; in the opposite case  $\mathbf{v}'$  is accepted only with the probability  $\Omega(\mathbf{v}')/\Omega(\mathbf{v})$ , and otherwise the current index  $\mathbf{v}$  is repeated. Thus, generally, the Metropolis probability for making the proposed shape change, i.e., moving from the current lattice site  $\mathbf{v}$  to the candidate site  $\mathbf{v}'$ , is given by

$$P(\mathbf{v} \rightarrow \mathbf{v}') = \min[1, \Omega(\mathbf{v}')/\Omega(\mathbf{v})]. \quad (16)$$

Were it not for the energy dependence of the microscopic effects, one would implement this procedure as follows. The statistical weight of a given lattice point is proportional to the nuclear level density for the corresponding shape, evaluated at the associated local excitation energy,  $\Omega(\mathbf{v}) \sim \rho[E^*(\chi^{(\mathbf{v})})]$ . Therefore the ratio between the statistical weight of the candidate shape  $\chi'$  and that of the current shape  $\chi$  would be evaluated as

$$\begin{aligned} \ln \frac{\Omega'}{\Omega} &= \ln \rho[E^*(\chi')] - \ln \rho[E^*(\chi)] \\ &\approx \frac{\partial}{\partial \chi} \ln \rho[E^*(\chi)] \cdot \Delta \chi \\ &= \frac{\partial \ln \rho(E^*)}{\partial E^*} \frac{\partial E^*(\chi)}{\partial \chi} \cdot \Delta \chi \approx -\frac{\Delta U}{T}, \end{aligned} \quad (17)$$

where  $\Delta \chi \equiv \chi' - \chi$  is the proposed change in the shape coordinate and  $\Delta U \equiv U(\chi') - U(\chi) \approx \partial_\chi U \cdot \Delta \chi$  is the corresponding change in the potential energy. We have used that  $\partial \ln \rho(E^*)/\partial E^*$  is the inverse of the temperature  $T(E^*)$  and that  $\partial E^*(\chi)/\partial \chi$  equals  $-\partial U(\chi)/\partial \chi$  because  $U + E^* = E$ . Thus,  $P(\chi \rightarrow \chi') \approx \min[1, \exp(-\Delta U/T)]$ .

The energy dependence of the microscopic effects complicates the comparison of the weights considerably. However, it is possible to treat this more general case in an equally simple manner by utilizing the effective potential  $U_E(\chi)$  introduced in Eq. (4),

$$\begin{aligned} \ln \frac{\Omega'}{\Omega} &= \ln \rho_E(\chi') - \ln \rho_E(\chi) \approx \frac{\partial \ln \rho_E(\chi)}{\partial \chi} \cdot \Delta \chi \\ &= \frac{\partial \ln \tilde{\rho}(E_E^*)}{\partial E_E^*} \frac{\partial E_E^*(\chi)}{\partial \chi} \cdot \Delta \chi \approx -\frac{\Delta U_E}{T_{\text{eff}}}, \end{aligned} \quad (18)$$

i.e.,  $P(\chi \rightarrow \chi') \approx \min[1, \exp(-\Delta U_E/T_{\text{eff}})]$ . Here we have used that the first factor is the inverse of the effective

temperature introduced in Eq. (15) and that  $\partial_{\chi} E_E^*(\chi)$  equals  $-\partial U_E(\chi)/\partial \chi$  because  $U_E + E_E^* = E$ .

Thus, the random walk on the shape lattice can be performed in a manner similar to the energy-independent case (17), the only differences being that the potential  $U(\chi)$  is replaced by the effective potential  $U_E(\chi)$  and the temperature  $T(\chi)$  is replaced by the effective temperature  $T_{\text{eff}}(\chi)$ . This facilitates the numerical implementation of the energy dependence.

Because the Metropolis lattice walk ignores the specific structure of the dissipation tensor, the extracted yields may generally depend somewhat on the specific manner in which a neighboring lattice site is selected. However, as illustrated in Ref. [2], this dependence is relatively insignificant, and our standard treatment considers all neighbors in the circumscribed 5D hypercube (so a given lattice site has a total of 242 immediate neighbors, except at the edges of the lattice).

#### D. Suppression function

We now turn to the determination of the key quantity, the suppression function  $S(E^*)$ .

Ignatyuk *et al.* [14] wrote the level density on the form (11) using an energy-dependent level-density parameter of the form (12) with an exponential suppression function  $S(E^*) = \exp(-\gamma E^*)$ . Their analysis yielded the value  $\gamma = 1/(15.625 \text{ MeV})$  for the damping rate. More recent applications of that approach usually write  $\gamma = \gamma_0/A^{1/3}$  and adjust  $\gamma_0$  to the data being analyzed. For example, for  $^{234}\text{U}$  the Reference-Input-Parameter-Library-2 (RIPL-2) compilation [15] finds  $\gamma = 1/(18.957 \text{ MeV})$ , whereas, the RIPL-3 compilation [16] finds  $\gamma = 1/(15.016 \text{ MeV})$ .

Therefore, for our present purposes, we first consider a purely exponential suppression function,  $S(E^*) = \exp(-E^*/E_0)$ . For fission of  $^{234}\text{U}$  at  $E^* = 11 \text{ MeV}$ , we show

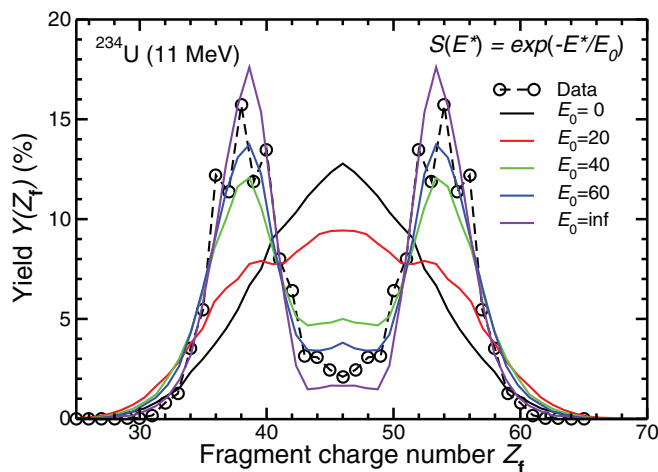


FIG. 2. (Color online) The relative fragment charge yield for fission of  $^{234}\text{U}$  at  $E^* = 11 \text{ MeV}$  as calculated with a purely exponential suppression function for various values of the damping energy  $E_0$  (indicated in MeV). The experimental data for  $^{234}\text{U}(\gamma, f)$  are from Ref. [17]. [The curve labeled “ $E_0 = 0$ ” was obtained for a purely macroscopic potential,  $U = U_{\text{macro}}$ .]

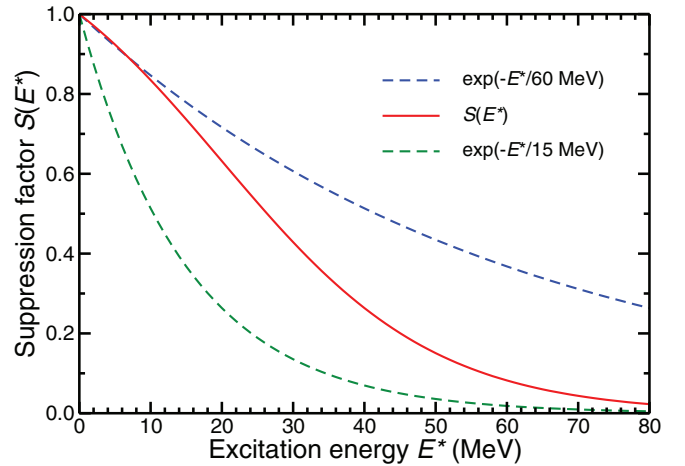


FIG. 3. (Color online) The suppression factor given in Eq. (19) with  $E_0 = 15 \text{ MeV}$  and  $E_1 = 20 \text{ MeV}$  together with two purely exponential forms,  $S(E^*) = \exp(-E^*/E_0)$ , that have either  $E_0 = 15 \text{ MeV}$  or  $E_0 = 60 \text{ MeV}$ .

in Fig. 2 the calculated mass yields for a wide range of damping energies  $E_0$  together with the experimental  $^{234}\text{U}(\gamma, f)$  data [17]. It is apparent that  $E_0$  values in the range of 15–20 MeV are far too small, leading to mass yields that are peaked at symmetry. A reasonably good reproduction of the experimental data is obtained for  $E_0 = 60 \text{ MeV}$ , whereas  $E_0$  values below 40 MeV lead to significant discrepancies. It is thus evident that if the suppression function is purely exponential then a reasonable reproduction of the fission-fragment yields can be obtained only if the associated damping energy is significantly larger than the values previously obtained from neutron-resonance analyses [14–16]. However, the use of a purely exponential suppression with  $E_0 = 60 \text{ MeV}$  would cause the microscopic effects to persist up to rather high

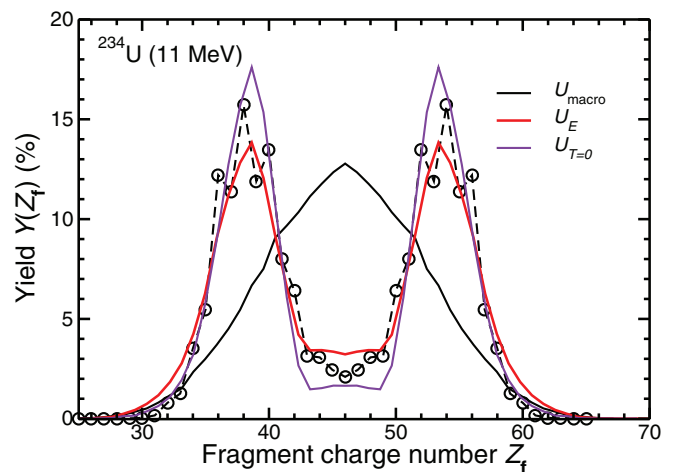


FIG. 4. (Color online) Similar to Fig. 2, but the charge yield has been calculated with either the energy-independent potential  $U_{T=0} = U_{\text{macro}} + U_{\text{sh+pair}}$  (corresponding to  $E_0 = \infty$  in Fig. 2) or the purely macroscopic potential  $U_{\text{macro}}$  ( $E_0 = 0$  in Fig. 2) as well as with the effective potential  $U_E$  (4) using the suppression function (19) with  $E_0 = 15 \text{ MeV}$  and  $E_1 = 20 \text{ MeV}$ .

excitations and, as a result, the mass yields would retain an asymmetric character even above  $E^* \approx 50$  MeV. We therefore adopt a modified functional form, namely a (renormalized) Woods-Saxon function,

$$S(E^*) = \frac{1 + e^{-E_1/E_0}}{1 + e^{(E^* - E_1)/E_0}} = \frac{1 + c}{e^{E^*/E_0} + c}. \quad (19)$$

The numerator in the center expression serves to ensure that  $S(0)$  is unity, and in the last expression we have introduced the constant  $c = \exp(E_1/E_0)$  for convenience. The purely exponential form is recovered for  $c = 0$ , which corresponds to  $E_1/E_0 \rightarrow -\infty$ , and the inverse of the initial slope is  $1/S'(0) = -(1 + c)E_0$ .

To determine the two parameters, we assume that the damping energy  $E_0$  has a value in the 15–20-MeV range, consistent with the analyses mentioned above, while we consider the energy shift  $E_1$  as adjustable. As a reminder that our approach is approximate and that the existing data do not permit a very accurate parameter determination, we select round values. We have adopted  $E_0 = 15$  MeV (the most recent value of the Ignatyuk damping energy [16]) and  $E_1 = 20$  MeV. This suppression function is shown in Fig. 3 together with the purely exponential form with either  $E_0 = 15$  MeV or  $E_0 = 60$  MeV. It follows the latter function quite closely up to  $E^* \approx 10$  MeV, while it drops off as  $\exp[-E^*/(15 \text{ MeV})]$  at high excitations.

As shown in Fig. 4, the modified suppression function (19) leads to a satisfactory reproduction of the observed mass yield for the  $^{234}\text{U}(\gamma, f)$  case, similar to what was obtained with  $\exp[-E^*/(60 \text{ MeV})]$  (see Fig. 2).

#### IV. BENCHMARKING

About a dozen years ago, Schmidt *et al.* [17] used the secondary-beam facility at GSI to study fission from 70 short-lived radioactive isotopes. A primary beam of 1-A-GeV  $^{238}\text{U}$  was fragmented on a beryllium target, and the resulting relativistic nuclei were then mass and charge analyzed in the fragment separator FRS [18]. These secondary beams were subsequently excited by electromagnetic interactions in a secondary lead target, mostly via the giant dipole resonance, leading to fission from a range of excitation energies centered at 11 MeV.

Here, we benchmark our calculated fragment distributions against those seminal data. For each of those 70 cases, we employ the Metropolis walk to calculate the fission-fragment charge distribution [obtained by a simple scaling of the mass distribution,  $P(Z_f) = P(A_f)A_0/Z_0$ ] for just a single excitation energy  $E^* = 11$  MeV, which represents a rough average of the experimentally generated excitations. However, for the lighter systems the fission barrier is often higher than 11 MeV. Because the observed fission events mainly originate from compound systems excited to energies above the saddle energy, we perform the calculations at excitation energies of 11 MeV or barrier height plus 2 MeV, whichever is higher. As has been pointed out previously, our method only applies to energies above the barrier. In practice, we cannot approach the saddle energy too closely because of the associated increase in the

computation time. Even at energies of 2 MeV above the saddle, the computation time can be several days for the 10 000 tracks we generate for this benchmark.

The experimental yields are contaminated by second and third chance fission to a level of approximately 15% and 5%, respectively [17]. Such contributions are not included in the calculated yields. The Metropolis walks are started from the ground-state shapes, but the results are not sensitive to the specific starting shape as long as it lies well inside the highest saddle.

The benchmark charge yields calculated with this standard treatment are displayed in Figs. 5–11 together with the data from Ref. [17]. The overall agreement between the calculated and the measured yields is very good, especially in regions where symmetric or asymmetric fission is well developed. It should be recalled that the measured yields display odd-even effects, a level of detail that is beyond the capability of the current models.

In the lighter mass region, the experimental yields tend to be symmetric, and the calculated yields reproduce this general feature. In particular, the widths of the distributions are matched quantitatively (see Figs. 5–7). Furthermore, the calculations tend to display slightly asymmetric charge yields for the lightest isotopes (Fig. 5), a feature also shown by very lightest measured yields.

In the heavier region, the measured yields begin to exhibit asymmetric components which gradually grow predominant, as is most clearly seen in the thorium and protactinium isotopic sequences. The calculated yields also display a gradual transition, but the individual cases have larger deviations, until the asymmetry has become well developed, at which point, the agreement is again quantitatively good. In the calculations, a relatively small asymmetric yield component appears too early (Fig. 8). Furthermore, the calculated asymmetric peaks seem to be located at a somewhat too large asymmetry, as was already discussed in Ref. [2] for  $^{226}\text{Th}$ .

To provide a global view of the transition from symmetric fission for the lighter nuclides to asymmetric fission for the very heaviest ones, we display in Fig. 12 the measured charge yields [17] together with the corresponding calculated yields. The layout is the same as that originally used in Ref. [17], except that the present subplots all have the same horizontal and vertical scales.

#### V. CONCLUDING REMARKS

We have previously shown that simple Metropolis random walks on five-dimensional macroscopic-microscopic potential-energy surfaces lead to overall remarkably good agreement with experimental data on fission-fragment mass (or charge) distributions [1]. Because those surfaces pertain to zero temperature, the treatment has been limited to relatively low excitations, such as fission induced by thermal neutrons.

We have now extended the treatment upwards in energy in a simple manner by means of effective potential-energy surfaces obtained by performing an energy-dependent suppression of the microscopic part of the potential energy of a given shape. With the adopted suppression function included, the resulting

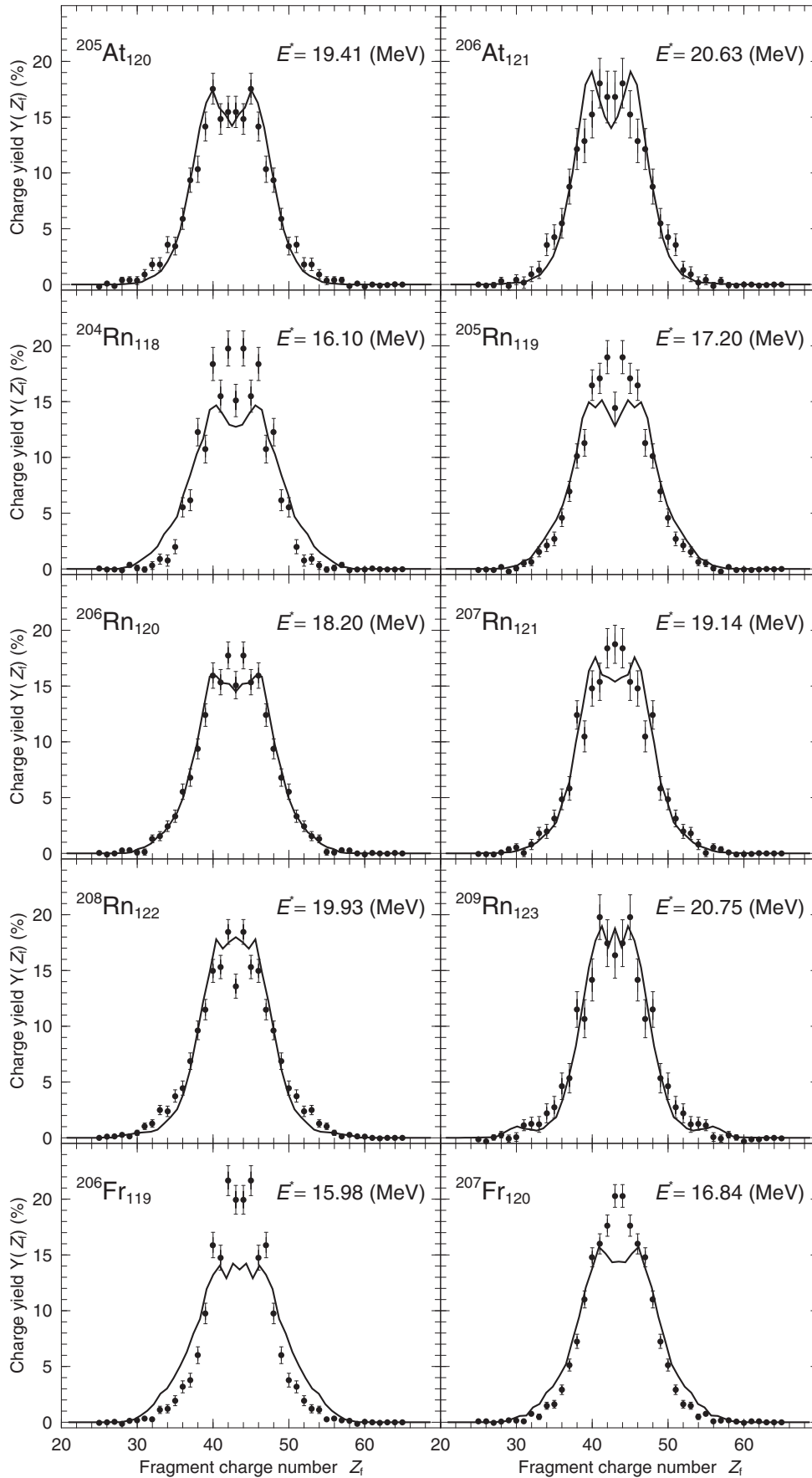


FIG. 5. Comparison of the calculated fission-fragment charge yields with the GSI data by Schmidt *et al.* [17] for cases 1–10.

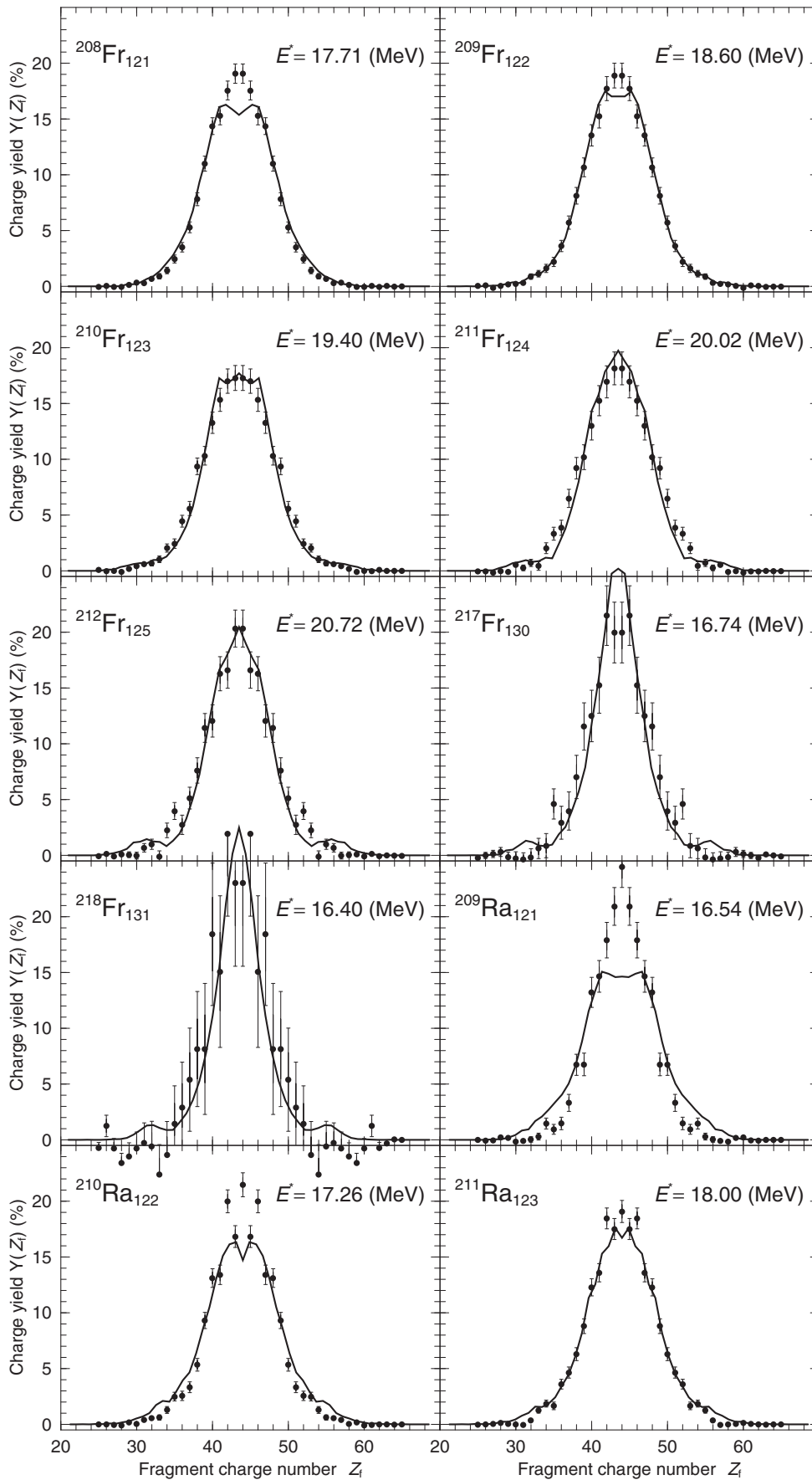


FIG. 6. Comparison of the calculated fission-fragment charge yields with the GSI data by Schmidt *et al.* [17] for cases 11–20.

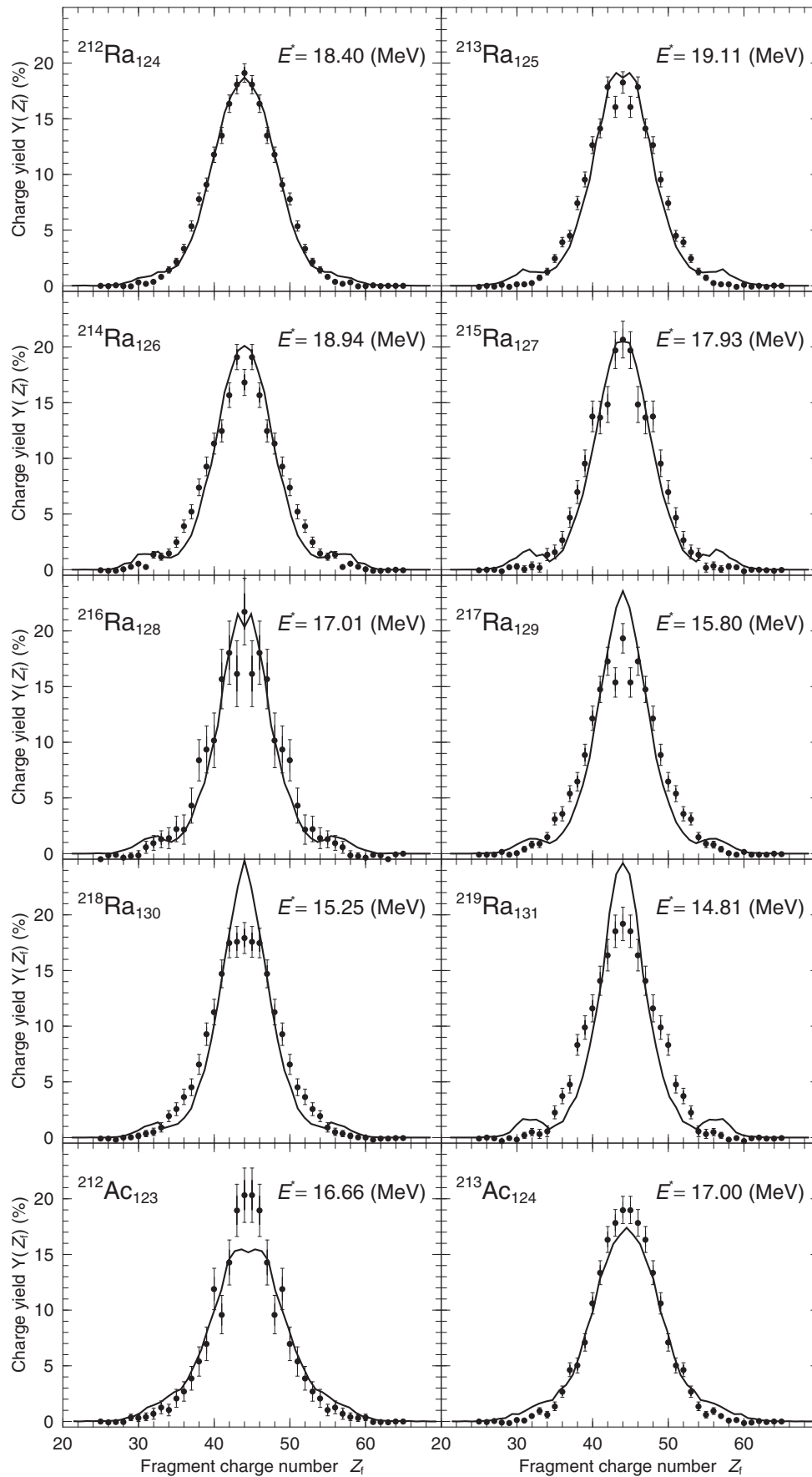


FIG. 7. Comparison of the calculated fission-fragment charge yields with the GSI data by Schmidt *et al.* [17] for cases 21–30.

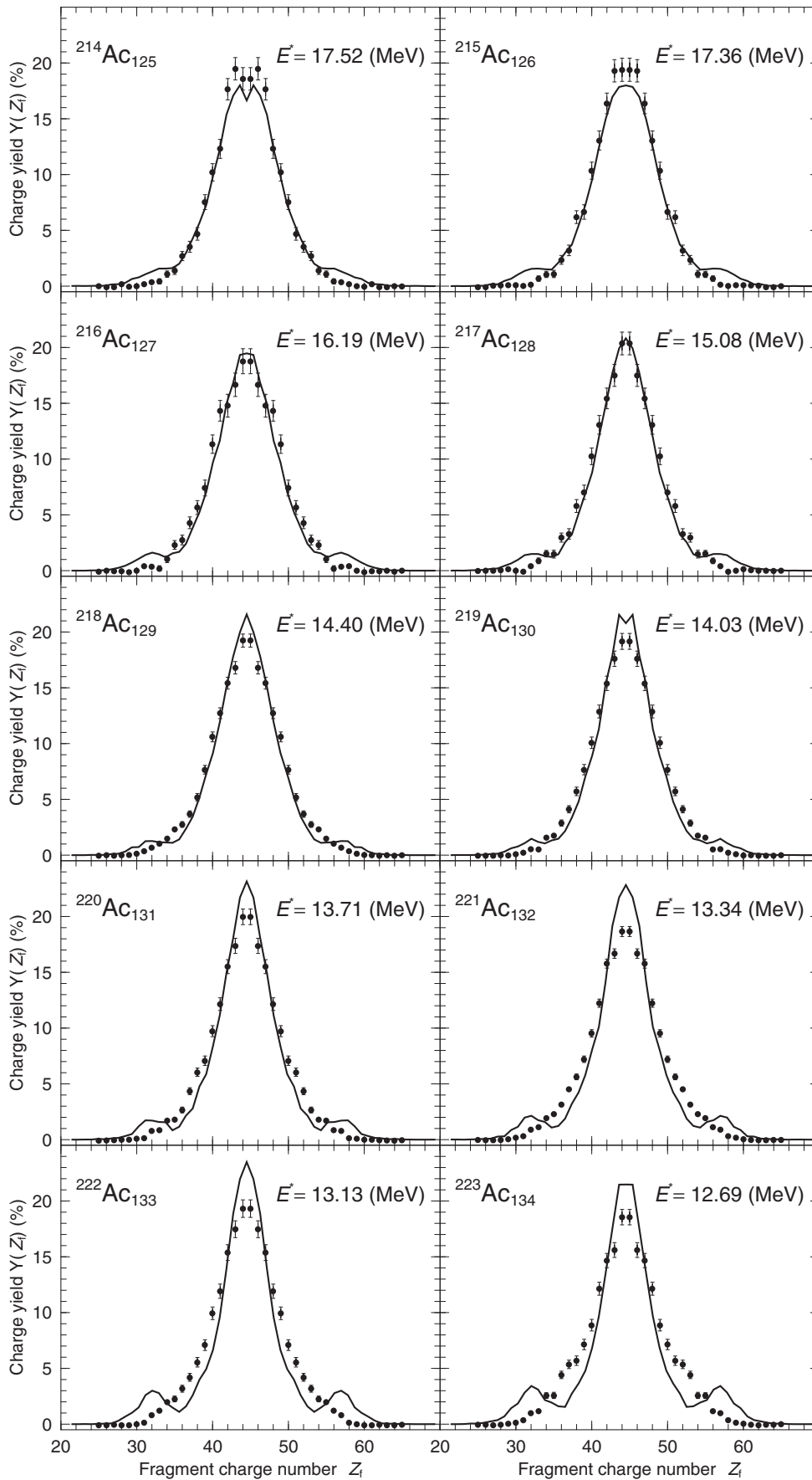


FIG. 8. Comparison of the calculated fission-fragment charge yields with the GSI data by Schmidt *et al.* [17] for cases 31–40.

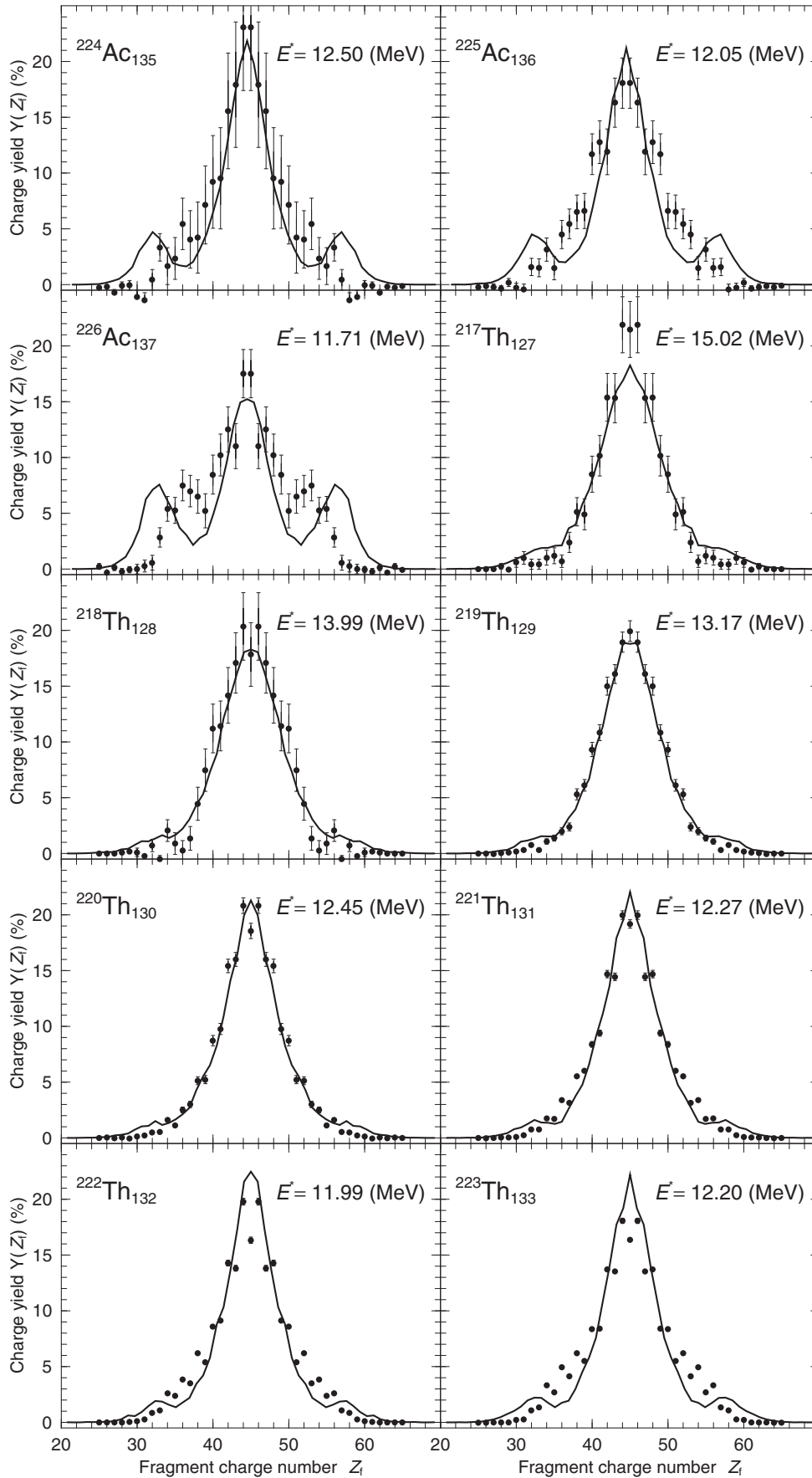


FIG. 9. Comparison of the calculated fission-fragment charge yields with the GSI data by Schmidt *et al.* [17] for cases 41–50.

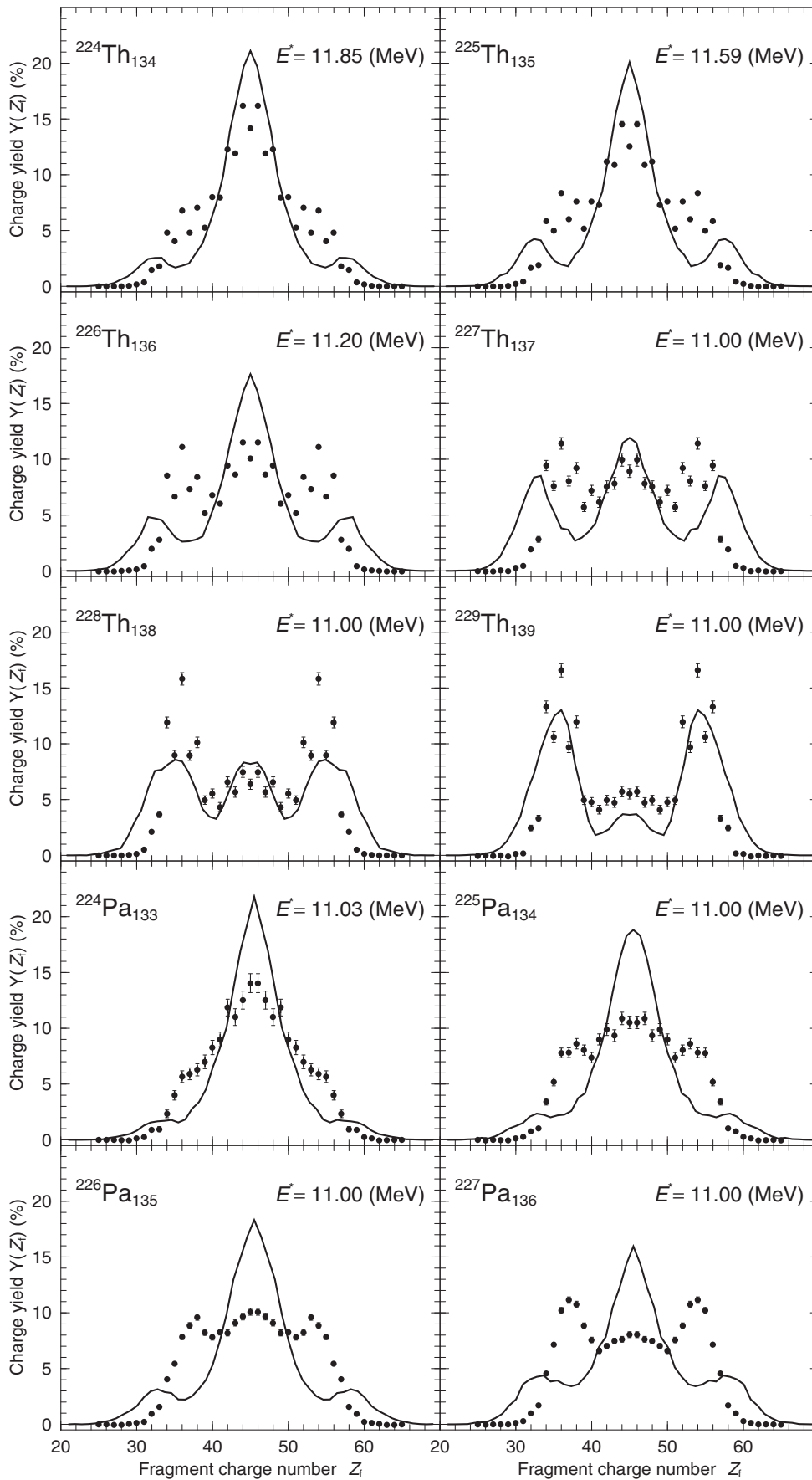


FIG. 10. Comparison of the calculated fission-fragment charge yields with the GSI data by Schmidt *et al.* [17] for cases 51–60.

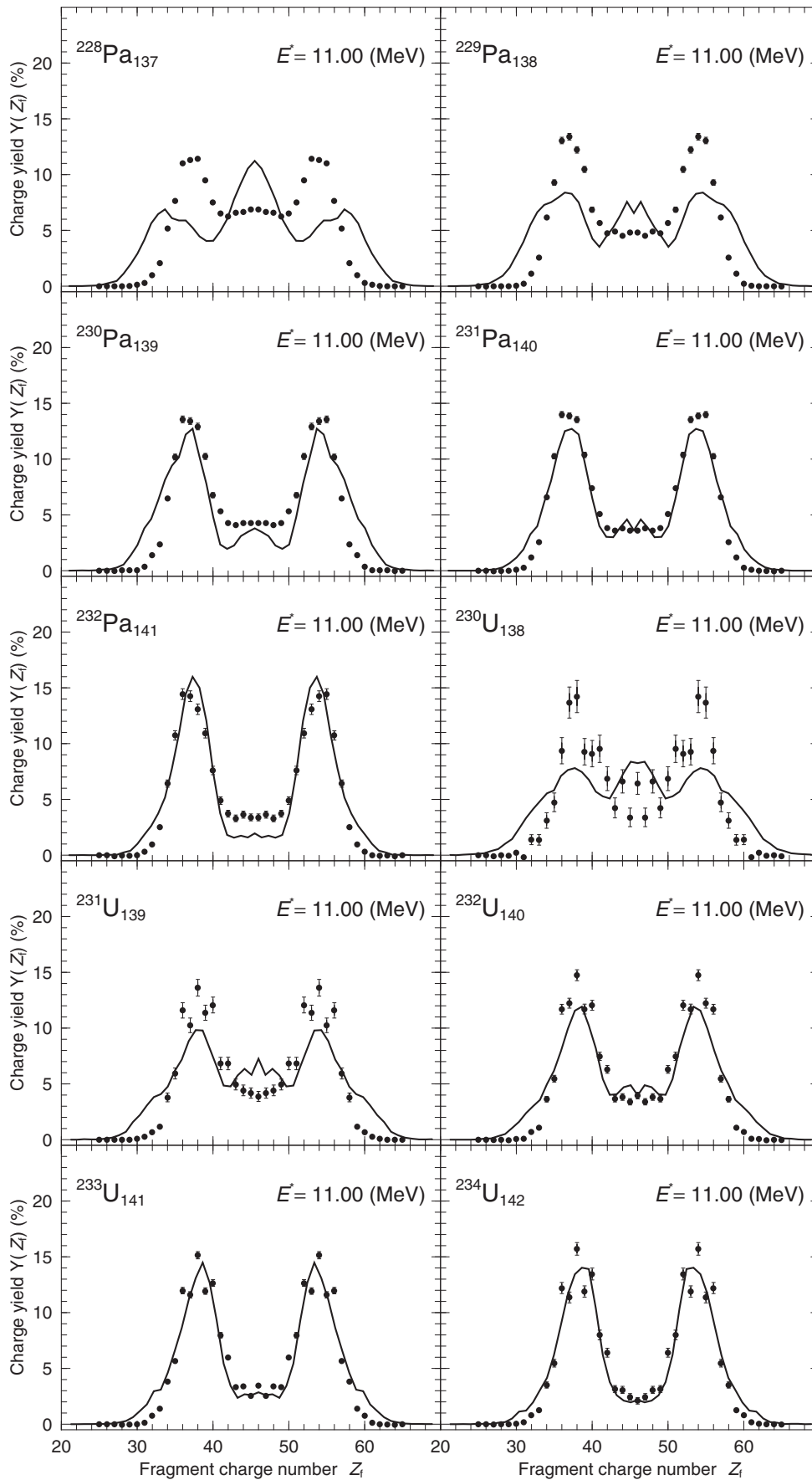


FIG. 11. Comparison of the calculated fission-fragment charge yields with the GSI data by Schmidt *et al.* [17] for cases 61–70.

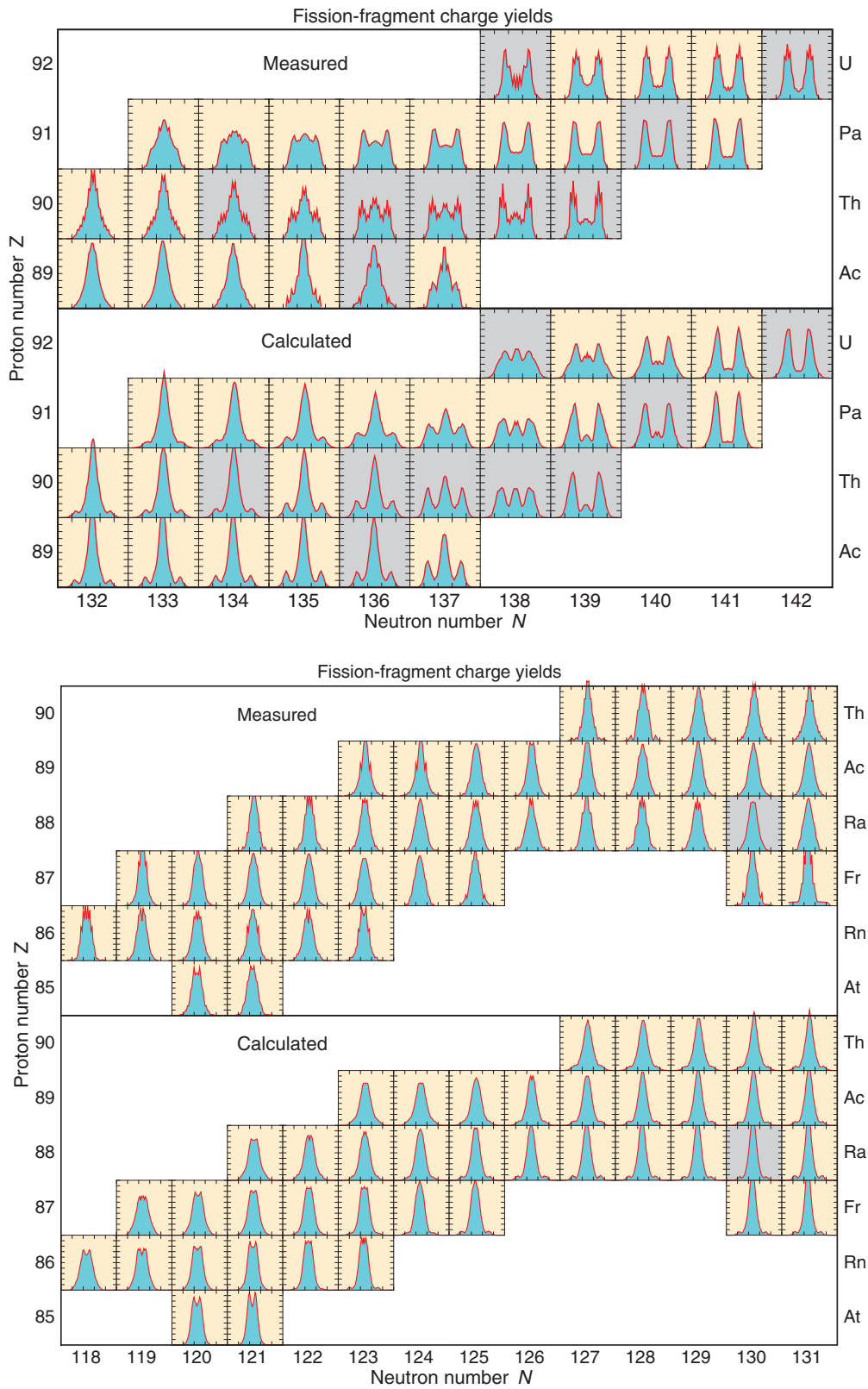


FIG. 12. (Color online) Comparison of the calculated fission-fragment charge yields with those measured by Schmidt *et al.* [17] for the elements that have  $Z = 85-90$  (lower panel) and  $Z = 89-92$  (upper panel), using the same layout as Fig. 20 in that paper. The subplots have horizontal axes covering  $Z = 20-70$ , with ticks for every ten units, and the vertical axes cover 0%–20%; the  $\beta$ -stable nuclei have gray backgrounds.

calculational method is then applicable up to high excitation energies where only the macroscopic part of the potential remains.

This refined treatment has been benchmarked against the 70 fission-fragment charge yields measured at GSI [17] several years ago, yielding an overall good agreement with the measured charged distributions. A benchmarking over such a wide region of the nuclear chart has not been performed for any other fragmentation yield model.

However, there are some obvious differences between the calculated yields and the observations in the transition region between asymmetric yields above  $A \approx 226$  and symmetric yields for lighter nuclei. But the transition region extends only across a range of four neutrons, for example from  $^{225}\text{Th}$  to  $^{229}\text{Th}$  in the case of thorium. This corresponds to just two neutron orbitals. The reproduction of the details of the observed transition between symmetric and asymmetric yields is comparable to the reproduction of the transition between spherical and deformed ground-state shapes near magic numbers where any global model may miss the transition location by several neutron orbitals [11,19,20]. Because the calculated yields in our model depend almost exclusively on the specific structure of the calculated potential-energy surface from approximately slightly inside the highest saddle point to scission, we may conclude that we have, for the first time in an extensive study, established that the calculated potential energy in this region of deformation is as realistic as near ground-state shapes.

Although the model has reproduced the observed fission yields for 70 heavy nuclei quite well, its “dynamical” aspects are remarkably simple. For example, the treatment does not require any assumptions about how the neck size affects the evolution of the mass asymmetry (one might expect changes in the mass asymmetry to be strongly hindered for small neck sizes). In the actinide region, the degree of asymmetry is governed mainly by the deep asymmetric valley in the

calculated potential-energy surface which often extends from the saddle region and all the way to scission [7,21]. One may therefore wonder how well the model would perform globally in regions with qualitatively different potential-energy surfaces, such as the mercury region [22] and, more generally, globally in the region  $74 \leq Z \leq 90$ . In this regard, it is noteworthy that the calculated fragment distribution for fission of  $^{180}\text{Hg}$  is asymmetric [3], as was observed via electron capture on  $^{180}\text{Tl}$  [23]. Some other data exist near  $A = 200$  [24,25] and elsewhere, but the experimental data are sparse and do not allow a systematic benchmarking of our current approach in this region.

Ideally, to draw firm conclusions about what model enhancements might be required, one would need to compare calculated yields to experimental data for long isotope sequences from the proton drip line to  $\beta$  stability or slightly beyond. We therefore encourage measurements in this region that are as comprehensive as those obtained in the GSI experiment [17].

#### ACKNOWLEDGMENTS

During this work, we have benefited from discussions with many colleagues, in particular, A. N. Andreyev, M. Brack, T. Døssing, F. Farget, H. Feldmeier, D. Hinde, T. Ichikawa, A. V. Ignatyuk, A. Iwamoto, K. Nishio, K.-H. Schmidt, A. J. Sierk, and R. Vogt. We also thank K.-H. Schmidt for providing computer-readable files of the experimental data in Ref. [17]. This work was supported by the Director, Office of Energy Research, Office of High Energy and Nuclear Physics, Nuclear Physics Division of the U.S. Department of Energy under Contract No. DE-AC02-05CH11231 (J.R.) and JUSTIPEN/UT Grant No. DE-FG02-06ER41407 (P.M.) and by the National Nuclear Security Administration of the U.S. Department of Energy at Los Alamos National Laboratory under Contract No. DE-AC52-06NA25396 (P.M.).

- 
- [1] J. Randrup and P. Möller, *Phys. Rev. Lett.* **106**, 132503 (2011).
- [2] J. Randrup, P. Möller, and A. J. Sierk, *Phys. Rev. C* **84**, 034613 (2011).
- [3] P. Möller, J. Randrup, and A. J. Sierk, *Phys. Rev. C* **85**, 024306 (2012).
- [4] G. D. Adeev, A. V. Karpov, P. N. Nadtochii, and D. V. Vanin, *Phys. Part. Nucl.* **36**, 712 (2005).
- [5] J. R. Nix, Report No. UCRL-17958 (unpublished), Lawrence Radiation Laboratory, University of California, July 1, 1968, expanded version of Ref. [6].
- [6] J. R. Nix, *Nucl. Phys.* **A130**, 241 (1969).
- [7] P. Möller, D. G. Madland, A. J. Sierk, and A. Iwamoto, *Nature (London)* **409**, 785 (2000).
- [8] W. J. Swiatecki, *Proceedings of the Second International Conference on Nuclidic Masses*, Vienna, Austria, July 15–19, 1963 (Springer, Berlin, 1963), p. 58.
- [9] V. M. Strutinsky, *Sov. J. Nucl. Phys.* **3**, 449 (1966).
- [10] N. Metropolis, A. W. Rosenbluth, M. N. Rosenbluth, A. H. Teller, and E. Teller, *J. Chem. Phys.* **26**, 1087 (1953).
- [11] P. Möller, J. R. Nix, W. D. Myers, and W. J. Swiatecki, *At. Data Nucl. Data Tables* **59**, 185 (1995).
- [12] P. Möller, A. J. Sierk, and A. Iwamoto, *Phys. Rev. Lett.* **92**, 072501 (2004).
- [13] K. H. Schmidt and B. Jurado, *Phys. Rev. C* **86**, 044322 (2012).
- [14] A. V. Ignatyuk, K. K. Istekov, and G. N. Smirenkin, *Sov. J. Nucl. Phys.* **29**, 450 (1979).
- [15] T. Belgya, O. Bersillon, R. Capote, T. Fukahori, Z. Ge, S. Goriely, M. Herman, A. V. Ignatyuk, S. Kailas, A. Koning, V. Plujko, and P. Young, IAEA Technical Report No. IAEA-TBCDOC-1506, 2006 (unpublished) (<http://www-nds.iaea.org/RIPL-2/>).
- [16] Capote *et al.*, *Nucl. Data Sheets* **110**, 3107 (2009).
- [17] K.-H. Schmidt *et al.*, *Nucl. Phys.* **A665**, 221 (2000).
- [18] H. Geissel *et al.*, *Nucl. Instrum. Methods B* **70**, 286 (1992).
- [19] S. Raman, C. W. Nestor, Jr., and P. Tikkanen, *At. Data Nucl. Data Tables* **78**, 1 (2001).
- [20] S. Goriely, F. Tondeur, and J. M. Pearson, *At. Data Nucl. Data Tables* **77**, 311 (2001).

- [21] P. Möller, A. J. Sierk, T. Ichikawa, A. Iwamoto, R. Bengtsson, H. Uhrenholt, and S. Åberg, *Phys. Rev. C* **79**, 064304 (2009).
- [22] T. Ichikawa, A. Iwamoto, P. Möller, and A. J. Sierk, *Phys. Rev. C* **86**, 024610 (2012).
- [23] A. N. Andreyev *et al.*, *Phys. Rev. Lett.* **105**, 252502 (2010).
- [24] M. G. Itkis, N. A. Kondrat'ev, S. I. Mul'gin, V. N. Okolovich, A. Y. Rusanov, and G. N. Smirenkin, *Yad. Fiz.* **52**, 944 (1990).
- [25] M. G. Itkis, N. A. Kondrat'ev, S. I. Mul'gin, V. N. Okolovich, A. Y. Rusanov, and G. N. Smirenkin, *Yad. Fiz.* **53**, 1225 (1991).